Ceramic binder jetting additive manufacturing: Effects of granulation on properties of feedstock powder and printed and sintered parts

Guanxiong Miao[a], Wenchao Du[b], Mohammadamin Moghadasi[c], Zhijian Pei[b], Chao Ma[a,b,c,d,*]

[a] Department of Mechanical Engineering, Texas A&M University, College Station, TX, US

[b] Department of Industrial and Systems Engineering, Texas A&M University, College Station, TX, US

[c] Department of Materials Science and Engineering, Texas A&M University, College Station, TX, US

[d] Department of Engineering Technology and Industrial Distribution, Texas A&M University, College Station, TX, US

* Corresponding author. E-mail address: cma@tamu.edu (Chao Ma)

Abstract

Because of the high sinterability, nanopowder could be beneficial for ceramic binder jetting additive manufacturing to achieve a high density on printed and sintered parts. However, the flowability of the nanopowder is poor because of the large interparticle cohesion. This poor flowability prohibits the usage of nanopowder in ceramic binder jetting. In this study, to improve the flowability of nanopowder, alumina nanoparticles are granulated into micron-sized granules through spray freeze drying. The raw nanopowder and granulated powder are compared by characterizing their flowability and printability. Results show that the granulated powder has a much better flowability than the raw nanopowder. Because of the superior flowability, the granulated powder forms a denser and smoother powder bed than the nanopowder which results in the higher density and smoother surface of the printed and sintered samples. The improvement on the final part quality indicates that the printability of the nanoparticles was improved by granulation.

Keywords

Additive manufacturing; binder jetting; ceramics; granulation; density

1. Introduction

Ceramic materials have widespread applications in the biomedical, aerospace, and chemical industries because of its outstanding biocompatibility, extraordinary resistance to wear, heat, and corrosion, and exceptional hardness. However, these excellent properties also make it difficult to fabricate ceramic materials into complex shapes using the conventional manufacturing techniques. In recent decades, additive manufacturing has been proved to be promising to fabricate ceramic materials into nearly any geometries with less tooling and more efficient usage of raw material [1, 2].

Binder jetting is an additive manufacturing process featured with a unique combination of advantages [1-14]. Firstly, no explicit support structures are needed for overhang structures in binder jetting because the loose powder supports them. Secondly, binder jetting is easy to scale up because numerous nozzles can be employed in a single print head. Thirdly, the debinding step is fast (compared with vat photopolymerization for example) because the amount of binder contained in the green part is low. Lastly, heat is uniformly applied in the consolidation step, avoiding the thermal shock, as seen in directed energy deposition for example.

However, the low density of the printed and sintered parts prohibits the application of binder jetting technology to ceramic materials [1, 3]. This low density is mainly caused by the contradictory requirements on the particle size of the feedstock powder: a large particle size is required to have a high flowability while a small particle size is required to achieve a high sinterability [1, 3].

To address the low density issue, mixing powders of different sizes has been investigated [11, 15, 16]. Because small particles can fill the vacancies between large particles, the density of the printed part can be improved. However, mixing powders of different sizes will often cause segregation which may affect the quality of the final part [17]. Efforts have also been made to improve the final part density by adding nanoparticles into the binder [18-23]. By jetting the modified binder onto the powder bed, nanoparticles can fill the vacancies between large particles to improve the density of the final part. As a result, the mechanical strength can also be improved, and the shrinkage can be reduced [18]. However, the loading of the nanoparticles in the binder is limited by the print head and the viscosity of the binder. Meanwhile, the skeleton formed by large particles will also prevent further densification even though nanoparticles are added as densifiers [2].

An alternative method for density improvement is to use granulated powder that addresses the contradictory requirements on flowability and sinterability of the feedstock powder. The granulation methods that have been investigated to produce feedstock powder for binder jetting mainly include grinding [24, 25] and spray drying [8, 25-29]. These previous investigations mostly aimed to engineer the pore structures of the final parts by granulation. Differently, the present study aims to increase the density of printed and sintered parts. This aim could be better realized with an emerging granulation method, spray freeze drying [30]. Unlike the irregular-shaped or hollow-structured granules produced by grinding or spray drying, granules produced by spraying freeze drying are spherical-shaped and uniform-structured [31]. These characteristics could be helpful for increasing the density of printed and sintered parts. In this study, spray freeze drying is introduced to binder jetting additive manufacturing for the first time. Preliminary results about the effects of spray freeze drying on properties of feedstock powder and printed and sintered parts are presented.

2. Experimental methods

2.1 Materials

De-agglomerated alumina nanopowder (90-187125, Allied High Tech, CA, US) with a particle size of 300 nm was selected as the raw material. Dispersant (Dispex AA 4040 NS, BASF, Germany) was used to decrease the viscosity of the granulation suspension. A diethylene glycol binder (TB-31 N, MicroJet Technology, Taiwan) was used for printing.

2.2 Granulation

Ball milling was used to prepare the granulation suspension. Suspension composition and ball milling parameter are shown in Table 1. First, deionized water, dispersant, and alumina balls (6.35 mm in diameter) were mixed in a polyethylene bottle. The total amount of alumina nanopowder was equally divided into three parts, and each part was added to the bottle every 3 hours during the ball milling process. Afterward, the mixture was ball-milled (Laboratory Jar Rolling Mill, Paul O. Abbe, IL, US) for another 12 hours. Before spraying, the suspension was screened using a 250 μm sieve to remove any large clusters that may block the atomizing nozzle.

Table 1. Suspension content

Parameter	**Value**
Alumina concentration (vol.%)	30
Dispersant-to-suspension weight ratio	0.015:1
Ball-to-suspension weight ratio	1:1

The suspension then went through the spray freezing step. A schematic of the setup (LS-2, PowderPro AB, Sweden) is shown in Figure 1. The suspension was pumped to the atomizing nozzle at a feed rate of 0.5 L/h. Then the suspension was atomized into droplets by the compressed air (pressure drop was set to 0.2 bar). The droplets were frozen once they were sprayed into the liquid nitrogen. These frozen droplets were then transferred to a freeze drier (FreeZone 2.5L, Labconco, MO, US) for lyophilization at a pressure of 1.5 mbar for 12 hours. To obtain a suitable particle size for printing, the dried granules were sieved to a size range of 53–90 μm using a sieve shaker (AS 200, Retsch GmbH, Germany).

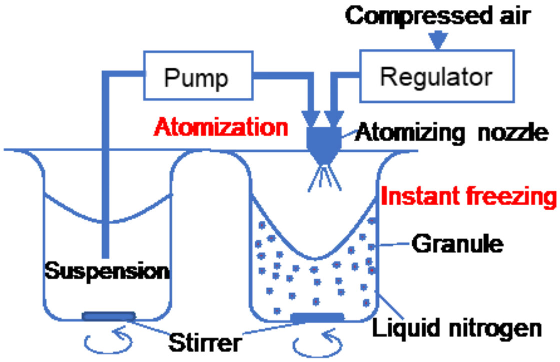

Figure 1. Schematic of spray freezing process

The morphology and size of the raw and granulated powders were characterized using scanning electron microscopy (SEM, FERA-3, TESCAN, Czech Republic). The particle size distribution of the granulated powder was obtained by analyzing the SEM images using ImageJ. The volume-weighted mean size (D) was calculated based on the following equation [32]:

$$D = \frac{\sum_{i=1}^{n} D_i \times V_i}{\sum_{i=1}^{n} V_i} \tag{1}$$

where n was the number of particles in the SEM image, and D_i and V_i were the diameter and volume of Particle *i*, respectively.

2.3 Flowability measurement

Flowability can be gauged by different metrics. In this research, mass flow rate, volumetric flow rate, apparent density, tap density, Hausner ratio, and Carr index, and repose angle were used to evaluate the flowability of the raw and granulated powders. Mass and volumetric flow rates were measured by a Hall flowmeter (DF-1-02, Hongtuo, Guangdong, China) following the ASTM B213-17 standard [33]. Apparent density (ρ_a) was measured by the Hall flowmeter following the ASTM B212-17 standard [34]. Tap density (ρ_t) was measured by a tap density tester (DY-100A, Daho Meter, Guangdong, China) following the ASTM B527-15 standard [35]. Hausner ratio (HR) and Carr index (CI) were determined by the following equations:

$$HR = \frac{\rho_t}{\rho_a} \tag{2}$$

$$CI = 100(1 - \frac{\rho_a}{\rho_t}) \tag{3}$$

Repose angle (RA) was also measured using the Hall flowmeter. The funnel was blocked first at the orifice and then fully filled with powder. Afterward, the powder was let flow, eventually forming a cone. With the diameter of the cone base (d) and the height of the cone (H) measured, repose angle was calculated using the following equation:

$$RA = \tan^{-1}(2H/d) \tag{4}$$

All the measurements were repeated three times.

2.4 Printability evaluation

The raw and granulated powders were printed with a commercial binder jetting 3D printer (ComeTrue T10, MicroJet Technology, Taiwan). For this printer, a counter-rotating roller is utilized to spread powder from the feed region to the build platform. A device for reduced build volume (RBV) was used to decrease the amount of powder needed for printing.

Powder bed density was the first metric to characterize the powder printability. A powder that can form a denser powder bed usually leads to a denser part. To measure the powder bed density, each powder was spread by the printer to form a powder bed with a thickness of 10 mm. The spreading parameters, are listed in Table 2. The layer thickness was selected to be bigger than the granule size to make sure no granules will be dragged by the roller. Traverse speed was selected to be the lowest speed because low speed can help to improve powder bed density [36-40]. Vender is the ratio of the amount of powder provided by the feed region to the amount of powder that the build platform can accommodate in each layer. A larger ratio means more powder is provided by the feed region. The vender value was set to 1.4 because the powder was enough to cover the whole powder bed in this condition. After spreading, the powder enclosed in the RBV was weighed, and the depth of the powder bed was measured with a caliper. In addition to the knowledge of the length and width of the powder bed, the powder bed density was obtained.

Table 2. Powder spreading and printing settings

Parameter	**Value**
Layer thickness (μm)	120
Roller rotation speed (RPM)	500
Roller traverse speed (mm/s)	30
Vender	1.4
Print time	2
Nozzle slot number	2

The bulk density of printed and sintered samples was determined to gauge the printability. Five cylindrical samples with a dimension of Ø6.35×12.7 mm were printed and sintered from each powder. The printing settings are listed in Table 2. Print time is the number of repetitive scans of the print head. A higher print time means more binder. Up to four nozzle slots are available on the print head to jet binder. Two nozzle slots were used in this work.

After cured at 35 °C for 3 hours, the samples went thought the debinding and sintering process. The debinding and sintering profile is shown in Figure 2. Firstly, the furnace was heated to 120 °C at a ramp rate of 1 °C/min. Then, the furnace was heated to 350 °C at a ramp rate of 5 °C/min, followed by debinding from 350 °C to 550 °C at a ramp rate of 1 °C/min. After debinding, the furnace temperature was increased to 1600 °C at a ramp rate of 5 °C/min. After sintered at 1600 °C for 2 hours, the samples were cooled to room temperature in the furnace.

The bulk volume of the printed and sintered samples (V_{prtS}) was determined based on the Archimedes' principle. The boiling method was adopted to ensure water completely filled the open pores: the samples were boiled in water for 3 hours and cooled down to room temperature [41]. After the boiling treatment, the mass of the immersed samples (m_i) was measured by suspending the samples in water. Then the mass of the soaked samples (m_s) was measured after the samples were taken out from the water and sponged with a wet absorbent cloth to remove any droplets on the surfaces. Based on these masses, the bulk volume of the samples was calculated using the following equation:

$$V_{prtS} = \frac{m_s - m_i}{\rho_{water}} \qquad (5)$$

where ρ_{water} was the theoretical density of water at room temperature. With the mass of the dry samples (m_d) measured, the printed and sintered bulk density (ρ_{prtS}) was determined. In addition, the printed and sintered apparent porosity (π_a), and printed and sintered closed porosity (π_c) were calculated using the following equations [41]. Here, the apparent porosity is defined as the ratio of volume of open pores to the bulk volume while the closed porosity is defined as the ratio of volume of closed pores to the bulk volume.

$$\pi_a = \frac{m_s - m_d}{m_s - m_i} \tag{6}$$

$$\pi_c = 1 - \frac{\rho_{prtS}}{\rho_{th}} - \pi_a \tag{7}$$

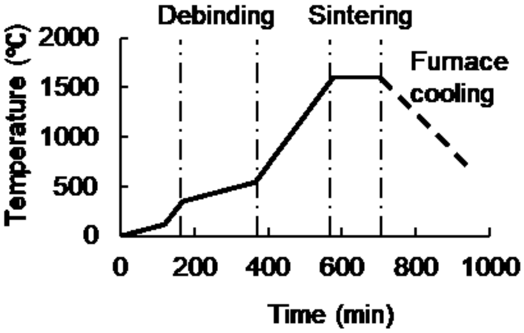

Figure 2. Debinding and sintering profile

To compare the microstructure, the printed and sintered samples were broken by bending them manually. Then the fracture surface was coated with platinum using a sputter coater (Cressington, Watford, UK) and characterized using SEM. The surface topography of the side surface of the printed samples was characterized using an optical profiler (ZeGage, Zygo, Connecticut, US).

3. Results and discussion

3.1 Powder morphology

Figure 3 shows the SEM images of the raw and granulated powders. The nanoparticles in the raw nanopowder (Figures 3a and 3b) have an irregular shape and form submicron agglomerates due to high interparticle cohesion. After granulation, all the granules are almost perfectly spherical, as shown in Figure 3c. The high sphericity was caused by the surface tension of the granulation suspension, which pulled the sprayed droplets into a spherical shape. This spherical shape was locked when the droplets were sprayed into liquid nitrogen and was maintained even after freeze drying because the water content was removed through sublimation, which did not involve melting or evaporation. The granule size and morphology could be controlled by process parameters such as spraying pressure and slurry feed rate. More details about the preparation of the granulated powder can be found elsewhere [30]. Figure 3d is the surface structure of an individual granule, which shows that the granules are formed by nanoparticles.

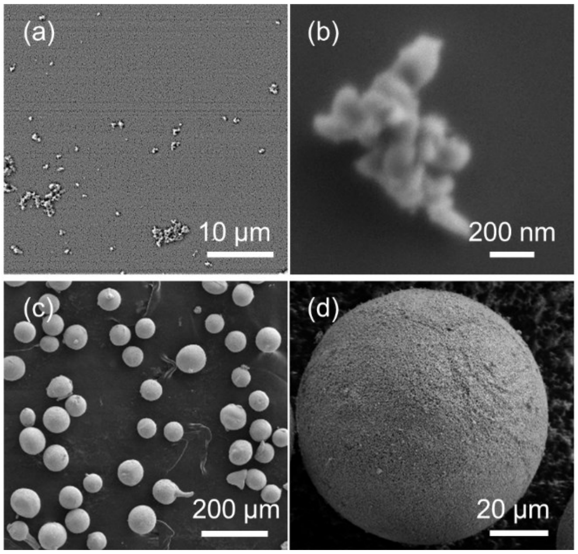

Figure 3. Morphology of (a) & (b) raw nanopowder and (c) & (d) granulated powder

Figure 4 is the particle size distribution of the granulated powder. All the particles are within the size range of 50–90 µm after sieving. The volume-weighted mean size of the granulated powder is 73.9 µm.

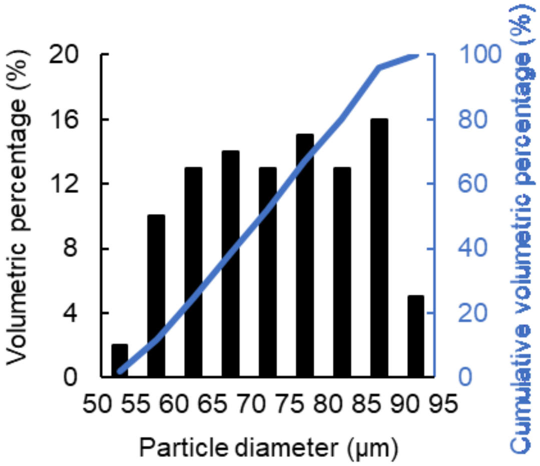

Figure 4. Particle size distribution of granulated powder

3.2 Flowability

Figure 5 shows the repose angle of the raw and granulated powders. The raw nanopowder has a much larger repose angle than the granulated powder. The larger repose angle was a result of the greater friction between particles that prevented them from sliding downwards on the cone surface, indicating a lower flowability.

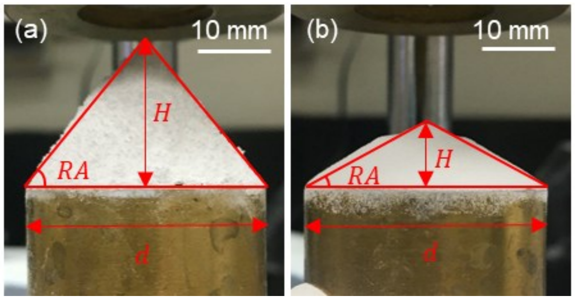

Figure 5. Repose angle of (a) raw nanopowder and (b) granulated powder

The flowability of the two powders was also evaluated by the apparent density, tap density, volumetric/mass flow rate, Hausner ratio, and Carr index. Table 3 listed all the values of the flowability metrics for the raw and granulated powders. The mass and volumetric flow rates of the raw nanopowder were not measurable because it could not freely flow through the Hall flowmeter. The other flowability metrics were normalized using the values of the raw nanopowder as the baseline and plotted in Figure 6.

Table 3. Flowability metric values of raw and granulated powders

Flowability metric	**Raw nanopowder**	**Granulated powder**
Volumetric flow rate (cm^3/s)	N/A	0.4 ± 0.0
Mass flow rate (g/s)	N/A	0.3 ± 0.001
Apparent density (%)	6.4 ± 0.0	15.6 ± 0.0
Tap density (%)	13.8 ± 0.2	18.8 ± 0.1
Hausner ratio	2.2 ± 0.8	1.2 ±0.0
Carr index	53.8 ± 0.8	17.1 ± 0.9
Repose angle (°)	52.6 ± 2.1	28.3 ± 0.6

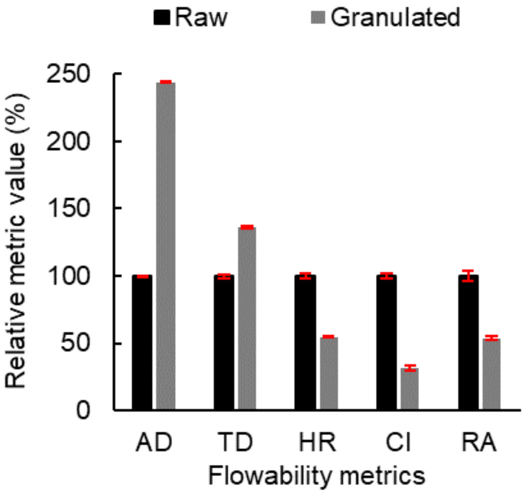

Figure 6. Relative flowability metric values of raw and granulated powders, including apparent density (AD), tap density (TD), Hausner ratio (HR), Carr index (CI), and repose angle (RA)

The granulated powder has a higher apparent density than the raw nanopowder. This is because, for nanoparticles, interparticle cohesion (e.g., van der Waals force and capillary force) is dominant compared to gravity [42-44]. Interparticle cohesion usually leads to severe agglomeration. These irregular-shaped agglomerates leave a great number of large inter-agglomerate pores in the powder after free settling, which leads to the lower apparent density. After tapping, the density changes more significantly for the raw nanopowder than the granulated powder, indicating the raw nanopowder is less packed after free settling. Both Hausner ratio and Carr index evaluate the difference between apparent density and tap density. A lower value of both Hausner ratio or Carr index indicates powder is less packed after free settling and thus has a lower flowability.

3.3 Printability

Figure 7 shows the surface of the powder bed formed by spreading the raw and granulated powders. It is obvious that the powder bed surface formed by the raw nanopowder is rough and has many voids. However, the powder bed obtained by granulated powder is smoother and more homogeneous. The superior powder bed quality of the granulated powder indicates that granulated powder has better printability and thus is more suitable for printing.

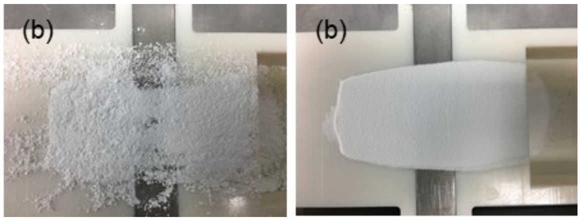

Figure 7. Powder bed surface quality of (a) raw nanopowder and (b) granulated powder

The printed and sintered samples made of both powders are shown in Figure 8. As a consequence of the poor powder quality, the sample printed with the raw nanopowder has a rougher surface and more cracks. By using the granulated powder as feedstock material, the surface roughness and dimensional accuracy were both improved.

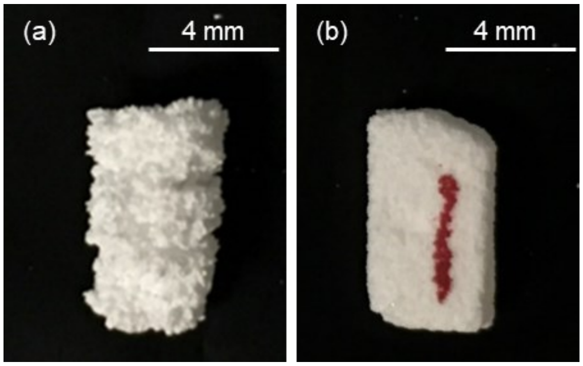

Figure 8. Printed and sintered samples from (a) raw nanopowder and (b) granulated powder

To compare the printability of both powders, powder bed density (relative), printed and sintered bulk density (relative), printed and sintered apparent porosity, and printed and sintered closed porosity are shown in Table 4 and Figure 9. Due to the spherical shape and better flowability, the powder bed density of the granulated powder is more than twice that of the raw nanopowder. The printed and sintered bulk density obtained by the granulated powder is more than 50% higher than that by the raw nanopowder. This is due to the higher powder bed density achieved by the granulated powder than the raw nanopowder. The samples from the raw nanopowder have a higher apparent porosity and the samples from the granulated powder have a higher closed porosity. The higher apparent porosity of the samples from the raw nanopowder may be because the powder bed is full of voids that form interconnected pores after sintering. The higher closed porosity of the samples from the granulated powder may be attributed to the porous structure of the spray-freeze-dried granules. The intragranular pores left by the sublimated water are isolated from the outside and probably evolve into closed pores after sintering.

Another observation that can be made based on Figure 9 is that the powder bed density of both powders is close to their apparent density and smaller than their tap density. Apparent and tap densities are usually used as the lower and upper limits of powder bed density [10]. The fact that the powder bed density is closer to the apparent density means the force provided by roller is very limited and not large enough to compact the powder.

Table 4. Printability metric values of raw and granulated powders

Metric	Raw nanopowder	Granulated powder
Power bed density (%)	6.0 ± 0.2	15.8 ± 0.1
Printed and sintered bulk density (%)	32.0 ± 1.4	50.7 ± 0.7
Printed and sintered apparent porosity (%)	64.6 ± 3.1	41.3 ± 2.0
Printed and sintered closed porosity (%)	3.4 ± 1.9	8.0 ± 1.6

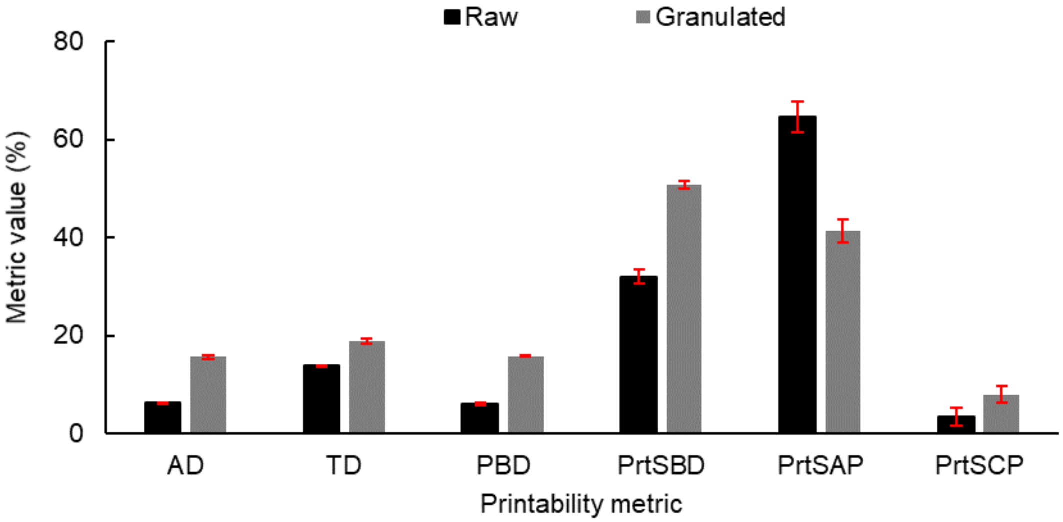

Figure 9. Printability metric values of raw and granulated powders, including powder bed density (PBD), printed and sintered bulk density (PrtSBD), printed and sintered apparent porosity (PrtSAP), and printed and sintered closed porosity (PrtSCP) in addition to apparent density (AD) and tap density (TD) of powders as references

Although the granulated powder has demonstrated a higher printed and sintered bulk density because of the higher flowability, the density still has a large room for improvement. The powder bed density achieved by the granulated powder is low (15.8%). The reason is the presence of both intragranular and intergranular pores. The following discussion is an attempt to estimate their contributions to the overall porosity. The (relative) density of the powder bed formed by the granulated powder (ρ'_{bed}) is determined by the packing density of the granules (ρ'_{interg}) within the powder bed and the packing density of nanoparticles within each granule (ρ'_{intrag}), as illustrated in Figure 10. The relation between these three densities is given by:

$$\rho'_{bed} = \rho'_{interg} \cdot \rho'_{intrag} \tag{8}$$

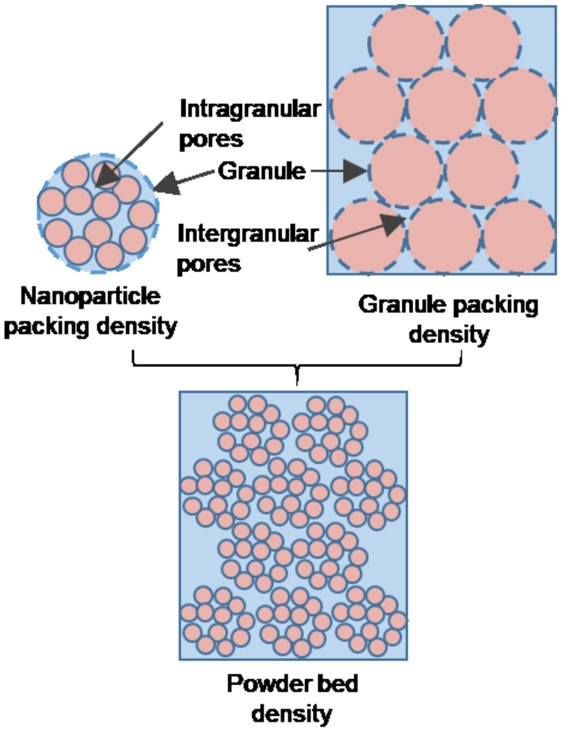

Figure 10. The packing structure of the granulated powder

The granulated powder is made by spray freeze drying from a suspension of the raw nanopowder with a solid loading of 30% by volume. After lyophilization, water inside a granule is removed, which leaves pores inside the granule. Therefore, the packing density of nanoparticles within each granule can be assumed to be 30% because the volume of the granule does not change much during lyophilization.

According to Eq (8), the packing density of the granules can be estimated to be 52.7%, which means intergranular porosity in the powder bed is as large as 47.3%.

To decrease or even eliminate the intragranular pores, the powder bed should be compacted to deform or break the granules. This strategy is highly possible by adding a compaction mechanism because of the low strength of the granules from spray freeze drying. Potential compaction methods include using forward-rotating roller [45], vibrating roller [46-48] or compression plate [49, 50]. More research is needed to explore the compaction force that can be provided by these different compaction methods and their influence on the powder bed density.

Figures 11 and 12 show the microstructure of printed and sintered samples from raw and granulated powders, respectively. As evidenced in Figures 11a and 12a, the nanoparticles in the raw nanopowder had been packed randomly with large pores connected to each other before sintering while the granules in the granulated powder packed regularly. This is the reason for the higher printed and sintered bulk density for the samples from the granulated powder. Comparing the higher-magnification images in Figures 11b and 12c, the microstructure of the granulated powder was similar to that of the raw nanopowder. The dense microstructure is a result of the excellent sinterability of the nanoparticles.

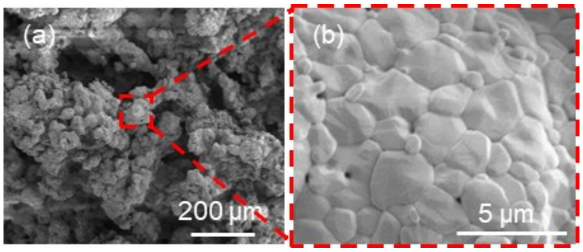

Figure 11. Printed and sintered microstructure from raw nanopowder

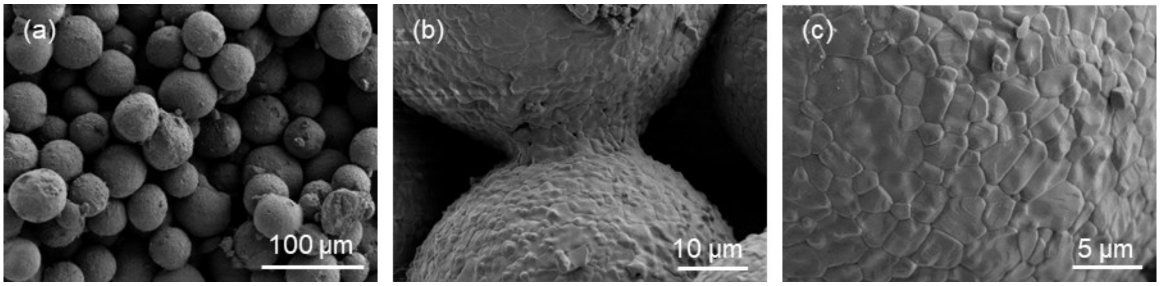

Figure 12. Printed and sintered microstructure from granulated powder

The surface topography of the printed and sintered samples from both powders are shown in Figure 13. The sample from the raw nanopowder has a much larger surface height variation (±300 μm) than that from the granulated powder (±100 μm). The sample from the raw nanopowder also has much larger pores than that from the granulated powder.

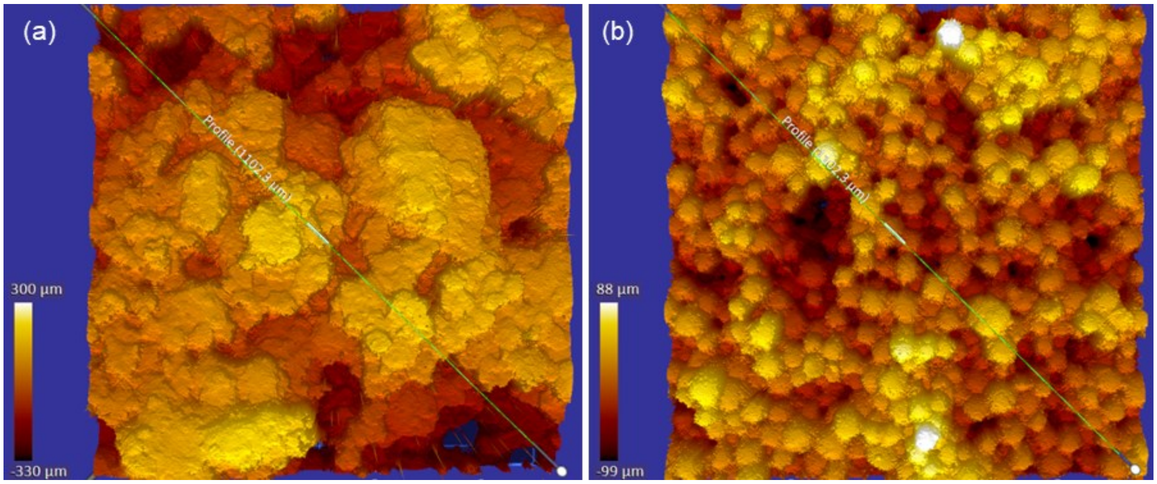

Figure 13. Surface topography of printed and sintered samples from (a) raw nanopowder and (b) granulated powder

5. Conclusions

The granulated powder is compared with the raw nanopowder in terms of flowability and printability. After granulation, the Hausner ratio was decreased from 2.2 ± 0.8 to 1.2 ± 0.0, the Carr index was decreased from 53.8 ± 0.8 to 17.1 ± 0.9, and the repose angle was decreased from 52.6 ± 2.1 to 28.3 ± 0.6. All these metrics indicate the flowability was significantly improved by granulation. For the printability, the powder bed formed by the granulated powder is smoother and denser, which leads to a more than 50% improvement of the printed and sintered bulk density. In conclusion, the granulated powder has a better flowability and printability than the raw nanopowder, resulting in higher density of printed and sintered samples.

Acknowledgement

This material is based upon work supported by the National Science Foundation under Grant No. 1762341.

References

[1] W. Du, X. Ren, Z. Pei, C. Ma, Ceramic Binder Jetting Additive Manufacturing: A Literature Review on Density, Journal of Manufacturing Science and Engineering 142(4), 2020.

[2] A. Mostafaei, A.M. Elliott, J.E. Barnes, C.L. Cramer, P. Nandwana, M. Chmielus, Binder Jet 3D Printing–Process Parameters, Materials, Properties, and Challenges, Progress in Materials Science, 2020.

[3] W. Du, X. Ren, C. Ma, Z. Pei, Binder Jetting Additive Manufacturing of Ceramics: A Literature Review, The ASME International Mechanical Engineering Congress and Exposition, Tampa, FL, US., 2017.

[4] M. Ziaee, N.B. Crane, Binder Jetting: A Review of Process, Materials, and Methods, Additive Manufacturing, 2019.

[5] M. Li, W. Du, A. Elwany, Z. Pei, C. Ma, Metal Binder Jetting Additive Manufacturing: A Literature Review, Journal of Manufacturing Science Engineering Fracture Mechanics, 2020, 1-45.

[6] L.A. Chavez, P. Ibave, B. Wilburn, D. Alexander, C. Stewart, R. Wicker, Y. Lin, The Influence of Printing Parameters, Post-Processing, and Testing Conditions on the Properties of Binder Jetting Additive Manufactured Functional Ceramics, Ceramics 3(1), 2020, 65-77.

[7] E. Sachs, M. Cima, J. Cornie, D. Brancazio, J. Bredt, A. Curodeau, T. Fan, S. Khanuja, A. Lauder, J. Lee, Three-Dimensional Printing: the Physics and Implications of Additive Manufacturing, CIRP Annals 42(1), 1993, 257-260.

[8] C.B. Williams, J.K. Cochran, D.W. Rosen, Additive Manufacturing of Metallic Cellular Materials via Three-Dimensional Printing, The International Journal of Advanced Manufacturing Technology 53(1-4), 2011, 231-239.

[9] N.D. Parab, J.E. Barnes, C. Zhao, R.W. Cunningham, K. Fezzaa, A.D. Rollett, T. Sun, Real Time Observation of Binder Jetting Printing Process Using High-Speed X-Ray Imaging, Scientific Reports 9(1), 2019, 1-10.

[10] H. Miyanaji, S. Zhang, L. Yang, A New Physics-Based Model for Equilibrium Saturation Determination in Binder Jetting Additive Manufacturing Process, International Journal of Machine Tools Manufacture 124, 2018, 1-11.

[11] W. Du, X. Ren, Y. Chen, C. Ma, M. Radovic, Z. Pei, Model Guided Mixing of Ceramic Powders with Graded Particle Sizes in Binder Jetting Additive Manufacturing, The ASME International Manufacturing Science and Engineering Conference, College Station, TX, US, 2018.

[12] W. Du, X. Ren, C. Ma, Z. Pei, Ceramic Binder Jetting Additive Manufacturing: Particle Coating for Increasing Powder Sinterability and Part Strength, Materials Letters 234, 2019, 327-330.

[13] M. Moghadasi, W. Du, M. Li, Z. Pei, C. Ma, Ceramic Binder Jetting Additive Manufacturing: Effects of Particle Size on Feedstock Powder and Final Part Properties, Ceramics International, 2020.

[14] ASTM International, 2012, ISO/ASTM 52900: Additive Manufacturing-General Principles-Terminology.

[15] Y. Bai, G. Wagner, C.B. Williams, Effect of Bimodal Powder Mixture on Powder Packing Density and Sintered Density in Binder Jetting of Metals, Solid Freeform Fabrication Symposium, Austin, TX, US, 2015.

[16] C. Sun, X. Tian, L. Wang, Y. Liu, C.M. Wirth, J. Günster, D. Li, Z. Jin, Effect of Particle Size Gradation on the Performance of Glass-Ceramic 3d Printing Process, Ceramics International 43(1), 2017, 578-584.

[17] H. Chen, Q. Wei, Y. Zhang, F. Chen, Y. Shi, W. Yan, Powder-Spreading Mechanisms in Powder-Bed-Based Additive Manufacturing: Experiments and Computational Modeling, Acta Material 179, 2019, 158-171.

[18] Y. Bai, C.B. Williams, The Effect of Inkjetted Nanoparticles on Metal Part Properties in Binder Jetting Additive Manufacturing, Nanotechnology 29(39), 2018, 395706.

[19] A. Bailey, A. Merriman, A. Elliott, M. Basti, Preliminary Testing of Nanoparticle Effectiveness in Binder Jetting Applications, International Solid Freeform Fabrication Symposium, 2016, pp. 1069-1077.

[20] H. Zhao, C. Ye, Z. Fan, C. Wang, 3D Printing of Cao-Based Ceramic Core Using Nanozirconia Suspension as a Binder, Journal of the European Ceramic Society 37(15), 2017, 5119-5125.

[21] Y. Bai, C.B. Williams, Binderless Jetting: Additive Manufacturing of Metal Parts via Jetting Nanoparticles, International Solid Freeform Fabrication, 2017.

[22] N.B. Crane, J. Wilkes, E. Sachs, S.M. Allen, Improving Accuracy of Powder‐Based SFF Processes by Metal Deposition From a Nanoparticle Dispersion, Rapid Prototyping Journal, 2006.

[23] P. Kunchala, K. Kappagantula, 3D Printing High Density Ceramics Using Binder Jetting With Nanoparticle Densifiers, Materials Design 155, 2018, 443-450.

[24] M. Ziaee, E.M. Tridas, N.B. Crane, Binder-Jet Printing of Fine Stainless Steel Powder with Varied Final Density, JOM 69(3), 2017, 592-596.

[25] J. Suwanprateeb, R. Sanngam, T. Panyathanmaporn, Influence of Raw Powder Preparation Routes on Properties of Hydroxyapatite Fabricated by 3D Printing Technique, Materials Science and Engineering: C 30(4), 2010, 610-617.

[26] P.H. Warnke, H. Seitz, F. Warnke, S.T. Becker, S. Sivananthan, E. Sherry, Q. Liu, J. Wiltfang, T. Douglas, Ceramic Scaffolds Produced by Computer‐Assisted 3D Printing and Sintering: Characterization and Biocompatibility Investigations, Journal of Biomedical Materials Research Part B: Applied Biomaterials 93(1), 2010, 212-217.

[27] M.N. Birkholz, G. Agrawal, C. Bergmann, R. Schröder, S.J. Lechner, A. Pich, H. Fischer, Calcium Phosphate/Microgel Composites for 3D Powderbed Printing of Ceramic Materials, Biomedical Engineering/Biomedizinische Technik 61(3), 2016, 267-279.

[28] M. Seidenstuecker, L. Kerr, A. Bernstein, H.O. Mayr, N.P. Suedkamp, R. Gadow, P. Krieg, S. Hernandez Latorre, R. Thomann, F. Syrowatka, 3D Powder Printed Bioglass and β-Tricalcium Phosphate Bone Scaffolds, Materials 11(1), 2018, 13.

[29] S.H. Irsen, B. Leukers, C. Höckling, C. Tille, H. Seitz, Bioceramic Granulates for Use in 3D Printing: Process Engineering Aspects, Materialwissenschaft und Werkstofftechnik: Entwicklung, Fertigung, Prüfung, Eigenschaften und Anwendungen technischer Werkstoffe 37(6), 2006, 533-537.

[30] W. Du, G. Miao, L. Liu, Z. Pei, C. Ma, Binder Jetting Additive Manufacturing of Ceramics: Feedstock Powder Preparation by Spray Freeze Granulation, The ASME International Manufacturing Science and Engineering Conference, Erie, PA, US, 2019.

[31] W. Du, G. Miao, L. Liu, Z. Pei, C. Ma, Binder Jetting Additive Manufacturing of Ceramics: Comparison of Flowability and Sinterability Between Raw and Granulated Powders, The ASME International Manufacturing Science and Engineering Conference, Erie, PA, US, 2019.

[32] ISO, 2014, 9276–2: 2014 Representation of Results of Particle Size Analysis–Part 2: Calculation of Average Particle Sizes.

[33] ASTM International, 2003, B213–03: Flow Rate of Metal Powders.

[34] ASTM International, 2017, B212-17: Standard Test Method for Apparent Density of Free-Flowing Metal Powders Using the Hall Flowmeter Funnel.

[35] ASTM International, 2015, B527-15: Standard Test Method for Tap Density of Metal Powders and Compounds.

[36] H. Chen, Y. Chen, Y. Liu, Q. Wei, Y. Shi, W. Yan, Packing Quality of Powder Layer during Counter-Rolling-Type Powder Spreading Process in Additive Manufacturing, International Journal of Machine Tools and Manufacture 153, 2020.

[37] L. Meyer, A. Wegner, G. Witt, Influence of the Ratio Between the Translation and Contra-Rotating Coating Mechanism on Different Laser Sintering Materials and Their Packing Density, International Solid Freeform Fabrication Symposium, Austin, TX, US, 2017.

[38] C. Meier, R. Weissbach, J. Weinberg, W.A. Wall, A.J. Hart, Critical Influences of Particle Size and Adhesion on the Powder Layer Uniformity in Metal Additive Manufacturing, Journal of Materials Processing Technology 266, 2019, 484-501.

[39] S. Haeri, Y. Wang, O. Ghita, J. Sun, Discrete Element Simulation and Experimental Study of Powder Spreading Process in Additive Manufacturing, Powder Technology 306, 2017, 45-54.

[40] Y.M. Fouda, A.E. Bayly, A DEM Study of Powder Spreading in Additive Layer Manufacturing, Granular Matter 22(1), 2020, 10.

[41] ISO, 2003, 18754: 2003 Fine Ceramics (Advanced Ceramics, Advanced Technical Ceramics)-Determination of Density and Apparent Porosity.

[42] G. Miao, W. Du, Z. Pei, C. Ma, Binder Jetting Additive Manufacturing of Ceramics: Analytical and Numerical Models for Powder Spreading Process, The ASME International Manufacturing Science and Engineering Conference, Erie, PA, US, 2019.

[43] E.J. Parteli, J. Schmidt, C. Blümel, K.-E. Wirth, W. Peukert, T. Pöschel, Attractive Particle Interaction Forces and Packing Density of Fine Glass Powders, Scientific Reports 4, 2014, 6227.

[44] L.I. Escano, N.D. Parab, L. Xiong, Q. Guo, C. Zhao, K. Fezzaa, W. Everhart, T. Sun, L. Chen, Revealing Particle-Scale Powder Spreading Dynamics in Powder-Bed-Based Additive Manufacturing Process by High-Speed X-Ray Imaging, Scientific Reports 8(1), 2018, 1-11.

[45] J. Yoo, M. Cima, S. Khanuja, Structural Ceramic Components by 3D Printing, Solid Freeform Fabrication Symposium, Austin, TX, US, 1993.

[46] S. Cao, Y. Qiu, X. Wei, H. Zhang, Experimental and Theoretical Investigation on Ultra-Thin Powder Layering in Three Dimensional Printing (3DP) by a Novel Double-Smoothing Mechanism, Journal of Materials Processing Technology 220, 2015, 231-242.

[47] S. Lee, Powder Layer Generation for Three Dimensional Printing, Massachusetts Institute of Technology, 1992.

[48] K.J. Seluga, Three Dimensional Printing by Vector Printing of Fine Metal Powders, Massachusetts Institute of Technology, 2001.

[49] J. Balistreri, J. Linder, K.A. Linder, G. Pugh, W. Bircher, T. Corp, Three-Dimensional (3D) Printing, U.S., 2019.

[50] L.N. Rabinskiy, S.A. Sitnikov, V.A. Pogodin, A.A. Ripetskiy, Y.O. Solyaev, Binder Jetting of Si3N4 Ceramics with Different Porosity, Solid State Phenomena 269, 2017, 37-50.